

# Solar light driven photoelectrocatalytic hydrogen evolution and dye degradation by metal-free few-layer MoS<sub>2</sub> nanoflower/TiO<sub>2</sub>(B) nanobelts heterostructure



Kamal Kumar Paul<sup>a</sup>, N. Srekanth<sup>b</sup>, Ravi K. Biroju<sup>b,1</sup>, Tharangattu N. Narayanan<sup>b</sup>, P.K. Giri<sup>a,c,\*</sup>

<sup>a</sup> Department of Physics, Indian Institute of Technology Guwahati, Guwahati 781039, India

<sup>b</sup> Tata Institute of Fundamental Research - Hyderabad, Sy. No. 36/P, Gopanapally Village, Serilingampally Mandal, Hyderabad 500107, India

<sup>c</sup> Centre for Nanotechnology, Indian Institute of Technology Guwahati, Guwahati 781039, India

## ARTICLE INFO

### Keywords:

MoS<sub>2</sub>/TiO<sub>2</sub> nanobelt  
Heterostructure  
Photocatalysis  
Dye degradation  
Photoelectrocatalysis  
Hydrogen evolution reaction

## ABSTRACT

A rational design of metal-free hierarchical nanostructures is critical for achieving next-generation photocatalytic system. Transition metal dichalcogenide, e.g., MoS<sub>2</sub> based heterostructures (HSs) with shape-controlled TiO<sub>2</sub> have attracted great attention in visible light electrocatalysis owing to their unique crystal structure, morphology and chemical properties. Herein, we demonstrate a low temperature solvothermal growth of few layer MoS<sub>2</sub> nanoflowers (NFs) over the porous TiO<sub>2</sub>(B) nanobelts (NBs) for enhanced hydrogen evolution reaction (HER) in acidic media as well as improved photocatalytic degradation of organic dye rhodamine-B (RhB) under visible light. Few-layer MoS<sub>2</sub> NFs with lateral sizes 130–350 nm were successfully grown on TiO<sub>2</sub> NBs, as revealed from the high resolution TEM imaging. EDS mapping confirms the elemental composition and their spatial distribution in the HS sample. MoS<sub>2</sub>/TiO<sub>2</sub> NBs HS exhibits extremely high adsorption ability (66% after 40 min) under dark as well as enhanced photocatalytic degradation efficiency (80% after 60 min) of RhB under visible light irradiation. A systematic photoelectrochemical measurements demonstrate that the MoS<sub>2</sub>/TiO<sub>2</sub> NBs HS exhibits excellent HER activity in acidic electrolyte with an overpotential and estimated Tafel slope to be –320 mV at 10 mA/cm<sup>2</sup> and 95 mV/dec, respectively, which is much lower than that of the pristine TiO<sub>2</sub> NBs measured to be –792 mV and 135 mV/dec, respectively, under visible light. It is shown that the Volmer-Heyrovsky mechanism leads to the extremely high hydrogen generation at the working electrode made with edge-defect enriched few layer MoS<sub>2</sub> on porous TiO<sub>2</sub> NBs.

## 1. Introduction

Ever increasing energy crisis and environmental pollution have necessitated the research efforts on the development of pollution free energy sources and practical solution to the everyday pollutions to the environment. Hydrogen is believed to be one of the most promising alternatives to fossil fuels and a source of renewable green energy having potential ability to replace the conventional energy sources in future. Solar light driven photocatalysis using semiconductor heterostructures (HSs) is one of the most promising green technologies for the generation of hydrogen by water splitting as well as remediation of environmental pollution [1–3]. After the pioneering work by Fujishima and Honda on the water splitting at the TiO<sub>2</sub> electrode in an electrochemical cell under the irradiation of UV light, hydrogen production using photoelectrocatalytic method by solar energy harvesting has

become a clean, economical and environment friendly approach [4]. Simultaneously TiO<sub>2</sub> and TiO<sub>2</sub> based nanostructures are being used for the decontamination of toxic and hazardous organic pollutants for the environmental protection [5–12]. To make the system commercially viable, the photocatalyst should be solar light active and efficient enough with high stability. To broaden the light harvesting window from UV to visible/NIR and uplift the catalytic activity, numerous strategies have been explored including impurity doping [13–15], staggered type HSs [1,5,16] and TiO<sub>2</sub> based plasmonic HSs with noble metal nanoparticles (NPs) [17–20] etc. Carbon nanotube coated with Cu<sub>2</sub>O [21], Fe-Pd alloy [22] can be a good photocatalyst. Synthesis of Fe<sub>3</sub>O<sub>4</sub>/ polyaniline by self-assembly approach, cobalt-based mixed oxide nanocrystals, edge-enriched graphene quantum dots and various core-shell nanostructures have recently been introduced for the efficient photocatalytic dye degradation, heavy metal removal, water oxidation

\* Corresponding author at: Department of Physics, Indian Institute of Technology Guwahati, Guwahati 781039, India.

E-mail address: [giri@iitg.ernet.in](mailto:giri@iitg.ernet.in) (P.K. Giri).

<sup>1</sup> Present address: Nanoscale Physics Research Laboratory, School of Physics and Astronomy, University of Birmingham, Birmingham B15 2TT, United Kingdom.

and supercapacitance [23–28]. In a suitable heterostructured system, the presence of heterojunction modifies the band positions as well as their inclination at the interface that accelerates the migration of photogenerated charge carriers through the heterojunctions, which eventually makes a photocatalyst highly efficient [29]. Therefore, incorporation of suitable co-catalysts like Pt, Pd, Ag, Au, Ru etc. and their oxide on the surfaces of TiO<sub>2</sub> can serve as catalytically active centers for the enhanced degradation of toxic pollutants as well as H<sub>2</sub> or O<sub>2</sub> generation [16,30,31]. However, extremely high cost and limited resources hinder their widespread use in commercial applications. To overcome these challenges, enormous effort has been paid towards the development of metal-free systems to achieve the enhanced catalytic performance. Discovery of graphene-based nanosheets [32–34] motivates more intense research on single/few-layer 2D transition metal chalcogenides. Among them, MoS<sub>2</sub> has now been recognized as an efficient co-catalyst [35] due to its structural anisotropy, chemical inertness and good electroconductivity [36]. The HER activity by MoS<sub>2</sub> nanosheets is limited on the edge-sites and vacancy sites, while the basal surface remains inert [37,38]. Thus, vacancy rich and maximally edge-exposed MoS<sub>2</sub> nanostructures are promising to grow in order to maximize the catalytic activity. When few-layer MoS<sub>2</sub> nanoflowers (NFs) are incorporated with the porous TiO<sub>2</sub> NBs, edge-rich MoS<sub>2</sub> with higher vacancy concentration is expected to be formed, with enhanced visible light absorption. Another way, MoS<sub>2</sub> and TiO<sub>2</sub> may form type-II heterojunction at their interfaces, facilitating easy and efficient migration of the photogenerated charge carriers from one semiconductor to another through the interface, which eventually boost the photocatalytic activity.

Recently, several studies have been reported on the photocatalytic hydrogen evolution and dye degradation using the MoS<sub>2</sub>/TiO<sub>2</sub> composites. Pourabbas et al. [39] have reported the photo-oxidation of phenol by MoS<sub>2</sub> NPs incorporated with ultrafine P25 TiO<sub>2</sub> from aqueous solution, while Xiang et al. [40] have demonstrated the hydrogen generation by TiO<sub>2</sub> NPs integrated with layered graphene and MoS<sub>2</sub> nanosheets under UV irradiation. Though the above mentioned systems exhibit superior photocatalytic activity, the ultra-small size of the nanocomposites (5–8 nm) suffers from the high collection cost after each cycle. Zhou et al. [1] and Li et al. [2] have modified the morphology of TiO<sub>2</sub> from its ultra-small spherical NPs to long nanobelts (NBs) and employed few layer MoS<sub>2</sub> nanosheets on them with high catalytic surface area, which in turn enhanced the hydrogen generation efficiency synergistically. Thus, a rational design of hierarchical nanostructures is crucial for achieving high efficiency photocatalytic and photoelectrocatalytic systems.

Herein, we report on the successful growth of pure TiO<sub>2</sub>(B) NBs via a solvothermal method and its in-situ surface decoration with few layer MoS<sub>2</sub> NFs by a 2nd stage hydrothermal method. The presence of edge-rich MoS<sub>2</sub> NFs on the porous TiO<sub>2</sub> NBs enhances the HER activity by photoelectrocatalytic water splitting as well as dye degradation efficiency under visible light. We demonstrate strong adsorption ability (66% after 40 min) as well as enhanced photocatalytic performance (80% after 60 min irradiation) in the decomposition of organic dye (RhB) by MoS<sub>2</sub>/TiO<sub>2</sub> HS under visible light irradiation. Additionally, HER activity of TiO<sub>2</sub> NBs greatly enhances after its integration with few layer MoS<sub>2</sub> NFs, which further increases after the irradiation with visible light. We show that the overpotential for TiO<sub>2</sub> is reduced considerably after the incorporation of MoS<sub>2</sub> under dark. Upon illumination with visible light, the charge transfer at the type-II heterojunction of MoS<sub>2</sub>/TiO<sub>2</sub> enhances, increasing the carrier density in the system which may be realized by the reduced charge transfer resistance. It is shown that the overpotential is substantially reduced in MoS<sub>2</sub>/TiO<sub>2</sub> under light irradiation. The mechanism of improved photoelectrocatalysis is discussed in details.

## 2. Experimental details

### 2.1. Materials

All the chemicals were used as-received without further purification. The purchased reagents are anatase TiO<sub>2</sub> powder (99%, Merck, India), ethylene glycol (99%, Merck, India), sodium hydroxide pellets (NaOH, 97%, Merck, India), sodium molybdate dihydrate (Na<sub>2</sub>MoO<sub>4</sub>·2H<sub>2</sub>O, 99%, Sigma-Aldrich, USA) and thioacetamide (C<sub>2</sub>H<sub>5</sub>NS, 99%, Titan Biotech Limited, India).

### 2.2. Preparation of TiO<sub>2</sub> NBs

Anatase TiO<sub>2</sub> nanopowder (average particle size ~ 80 nm), ethylene glycol and sodium hydroxide (NaOH) pellets were used in our experiments as received from Merck without any further purification. In a typical synthesis, 0.2 g of anatase TiO<sub>2</sub> powder was dispersed in a 50 ml of 10 M NaOH solvent prepared by mixing DI water and ethylene glycol in 1:1 volume ratio. Afterwards, the mixed TiO<sub>2</sub> solution was transferred into a Teflon-lined autoclave (Berghof, BR-100) and the inside temperature was maintained and monitored at 220 °C for 16 h with a constant magnetic stirring at 500 rpm. The treated precipitates were washed thoroughly with DI water and 0.1 N HCl until the pH reduces to 7, which confirms the complete exchange of Na<sup>+</sup> by H<sup>+</sup> ions. Then, the obtained H-titanate NBs were calcined at 500 °C for 5 h in ambient atmosphere to grow porous TiO<sub>2</sub>(B) NBs.

### 2.3. Growth of MoS<sub>2</sub>/TiO<sub>2</sub> NBs heterostructures

Typically, 20 mg of TiO<sub>2</sub>(B) NBs were dispersed into a 40 ml of MQ water in an ultrasonic bath for 30 min. Then, 60 mg sodium molybdate (Na<sub>2</sub>MoO<sub>4</sub>·2H<sub>2</sub>O) and 120 mg thioacetamide (C<sub>2</sub>H<sub>5</sub>NS) were dissolved in the above solution. The mixture was transferred to a Teflon-lined stainless steel autoclave and heated at 240 °C for 24 h with a constant magnetic stirring at 250 rpm. The amount of reagent was chosen and optimized based on the initial report by Zhou et al. [1]. The obtained black precipitates were washed several times with DI water for removing the additional salts and impurities followed by a centrifugation and drying process at 50 °C for 12 h to obtain few-layer MoS<sub>2</sub> NFs decorated on TiO<sub>2</sub> NBs (MoS<sub>2</sub>/TiO<sub>2</sub> HSs) with 1:1 weight of MoS<sub>2</sub> and TiO<sub>2</sub>. For comparison, pure MoS<sub>2</sub> NFs were synthesized under identical conditions without the presence of TiO<sub>2</sub> NB platform.

### 2.4. Characterization techniques

Morphology and size of the as-synthesized TiO<sub>2</sub> NBs and MoS<sub>2</sub> NFs on the TiO<sub>2</sub> NBs have been studied by a field emission scanning electron microscope (FESEM) (Sigma, Zeiss) equipped with an energy dispersive X-ray (EDX) spectrometer. The high magnification surface morphologies and structures of the as-grown samples have been studied by a field emission transmission electron microscope (FETEM) (JEOL-JEM 2100 F operated at 200 kV). Samples for TEM analysis have been prepared on a carbon coated Cu grid of 400 mesh size (Pacific Grid, USA). The crystal structure of the as-grown catalysts has been obtained from X-ray powder diffraction (XRD) pattern (Rigaku RINT 2500 TTRAX-III, Cu K $\alpha$  radiation). Crystallinity and phase composition of the as-synthesized NBs and the number of layers in MoS<sub>2</sub> NFs have been confirmed from the micro-Raman measurement (LabRam HR800, Jobin Yvon). The Fourier transform infrared (FTIR) spectra were measured for each of the catalysts in the range 400–4000 cm<sup>-1</sup> with a FTIR spectrometer (Perkin Elmer, Spectrum BX) using KBr wafer. X-ray photoelectron spectroscopy (XPS) has been carried out using a PHI X-tool automated photoelectron spectrometer (ULVAC-PHI, Japan) with an Al K $\alpha$  X-ray beam (1486.6 eV) at a beam current of 20 mA. The shift in the binding energy of various catalysts has been corrected using the C1s spectrum at 284.8 eV as a standard value [5]. Nitrogen adsorption-desorption

isotherms have been conducted by Quantachrome autosorb-iQ MP analyzer at 77 K. Multipoint Brunauer–Emmett–Teller (BET) method was applied to estimate the surface area of the catalysts and Barrett–Joyner–Halenda (BJH) model to determine the average pore size. UV–Vis diffuse reflectance spectroscopy (DRS) measurements of the samples were recorded using a commercial spectrophotometer SHIM-ADZU 2600.

### 2.5. Photocatalytic degradation under visible light

The photocatalytic activity of pure TiO<sub>2</sub>(B) NBs and MoS<sub>2</sub>/TiO<sub>2</sub>(B) HSs has been evaluated considering the photodegradation of Rhodamine-B (RhB) under visible light irradiation. In a typical experiment, 50 ml aqueous solution of RhB (30 mg/L) and 20 mg of catalyst powders have been placed in a 100 ml beaker. Prior to the irradiation, the mixture of dye solution and photocatalyst were magnetically stirred under dark for 40 min and during stirring 3 ml of dye solution was collected at a regular interval and centrifuged immediately to separate the catalyst and dye which prevents further adsorption. A 250 W lamp was used as the light source (emission range 370–730 nm) for visible light photocatalysis. The lamp is surrounded by a water-cooled quartz jacket which maintains the ambient temperature by absorbing the heat generated from the source. At 10 min irradiation intervals, 3 ml of solution was collected and centrifuged to remove the catalyst particles from the dye solution for further study. In order to estimate the degradation of dye in the solution, UV–Vis absorbance was measured in a Shimadzu 2450 UV–Vis spectrophotometer.

### 2.6. Photoelectrocatalysis measurements under visible light

Photoelectrochemical measurements were performed in a custom made electrochemical cell with three electrodes: a Pt wire as counter electrode, Ag/AgCl (saturated KCl) as reference electrode and TiO<sub>2</sub> or MoS<sub>2</sub>/TiO<sub>2</sub> with electrochemically active surface area  $\sim 0.05 \text{ cm}^2$  supported on a mechanically polished glassy carbon substrates as working electrode. The photoelectrocatalytic studies were carried out using a Bio Logic SP-300 electrochemical work station. A 300 W Xenon lamp (Lelesil Innovative Systems, India) with wavelength range  $\sim 370\text{--}730 \text{ nm}$  is used as the visible light source during the electrochemical measurements under light. Prior to the measurements, a nitrogen saturated 0.5 M H<sub>2</sub>SO<sub>4</sub> is used as electrolyte for all catalysts. The HER performance of our best catalyst, MoS<sub>2</sub>/TiO<sub>2</sub> was also measured in a different electrolyte solution 0.1 M NaOH (pH value  $\sim 12$ ). Linear sweep voltammetry (LSV) was conducted at a scan rate of  $10 \text{ mV s}^{-1}$ . Electrochemical impedance spectroscopy (EIS) was also measured in 0.5 M H<sub>2</sub>SO<sub>4</sub> over the frequency range 100 Hz–7 MHz with an input sine wave having 10 mV amplitude.

## 3. Results and discussion

### 3.1. Morphology studies

The growth of one dimensional TiO<sub>2</sub> nanostructures and its surface decoration by few layer MoS<sub>2</sub> by the hydrothermal process have been discussed by several groups [1,2]. The typical morphology and microstructural properties of TiO<sub>2</sub> NBs and MoS<sub>2</sub>/TiO<sub>2</sub> NB HSs were first characterized by FESEM. Fig. 1(a) depicts the FESEM image of porous TiO<sub>2</sub> NBs with diameter  $\sim 30\text{--}150 \text{ nm}$  and lengths up to a few  $\mu\text{m}$ . MoS<sub>2</sub> NFs from the self-assembly of few layer MoS<sub>2</sub> nanosheets have been grown successfully and almost uniformly on the TiO<sub>2</sub> NBs. Fig. 1(b) shows a FESEM image of uniform decoration of MoS<sub>2</sub> NFs over the TiO<sub>2</sub> NBs. The inset shows a magnified view of the MoS<sub>2</sub> NFs, which confirms the formation of rose like NFs with sizes in the range 130–350 nm. EDX analysis on the as-grown TiO<sub>2</sub> NBs and MoS<sub>2</sub>/TiO<sub>2</sub> NBs HS reveals that it contains Ti, O (in case of TiO<sub>2</sub> NBs) and Ti, O, Mo and S elements (in case of MoS<sub>2</sub>/TiO<sub>2</sub> NBs HS), as shown in Fig. 1(c),(d).

HRTEM was employed for the further characterization of the structures and surface morphologies of the HSs. Fig. 2(a) shows the TEM image of pristine TiO<sub>2</sub> NBs and it can be noted that the TiO<sub>2</sub> NBs are uniform in diameter and comprised with pores on its surface. It has been reported that porous structure in TiO<sub>2</sub> forms predominantly due to the dehydration reaction that took place for the phase transformation during the hydrothermal reaction [41]. These porous sites may act as a nucleation site for the growth of hybrid nanostructure of other material on TiO<sub>2</sub>. Fig. 2(b) reveals the in-situ growth of MoS<sub>2</sub> NFs on the porous TiO<sub>2</sub> NBs with a broad size distribution 100–380 nm, which is in good agreement with the value measured from FESEM analysis. Fig. 2(c) shows an enlarged view of a MoS<sub>2</sub> NF on the porous TiO<sub>2</sub> NB. It may be noted that after the decoration with MoS<sub>2</sub> NFs, the larger sized pores on TiO<sub>2</sub> surface appear to be occupied but not the smaller pores, as confirmed later from the BET analysis. As shown in Fig. 2(b),(c), the pure MoS<sub>2</sub> crystals appear to be few layer petals-like structures, which is wavy in nature, probably assemble together inside the autoclave with very high pressure ( $\sim 45 \text{ bar}$ ) to form discrete nanorose-like structures on the porous TiO<sub>2</sub> platform. Note that both MoS<sub>2</sub> and TiO<sub>2</sub> contain structural defects and strong interaction between these two materials may take place probably through the oxygen vacancy sites in TiO<sub>2</sub> and the sulfur atoms in MoS<sub>2</sub>. The strong coupling at the interface may thus result in a type-II heterojunction between MoS<sub>2</sub> and TiO<sub>2</sub>. It can be clearly observed from Fig. 2(d) that the layered MoS<sub>2</sub> nanosheet coexists with the TiO<sub>2</sub>. From the HRTEM image, the lattice fringes of the MoS<sub>2</sub> nanosheets and TiO<sub>2</sub> NBs can be clearly observed, which suggest the well-defined crystal structure of the nanostructure components. The fringes with lattice spacing of 0.68 nm correspond to the (002) planes of MoS<sub>2</sub>, and the lattice spacing of 0.39 nm corresponds to the (201) crystal planes of pure B-phase TiO<sub>2</sub>. It can be noted that the (002) plane of MoS<sub>2</sub> comprises of only 6 layers of MoS<sub>2</sub> nanosheets. In order to demonstrate the spatial distribution of each element in the HS, EDS elemental mapping analysis was performed. Fig. 2(e) shows a STEM image of MoS<sub>2</sub>/TiO<sub>2</sub> HS on which elemental mapping analysis was done. Fig. 2(f),(g) reveal that the core of the HS is comprised of Ti and O element, respectively which further confirms the uniform growth of TiO<sub>2</sub> platform. Fig. 2(h),(i) exhibit the elemental mapping for Mo and S, respectively, confirming the growth of discrete MoS<sub>2</sub> NFs on the TiO<sub>2</sub> platform as an outer layer.

### 3.2. Structural analysis

#### 3.2.1. XRD analysis

The X-ray powder diffraction (XRD) patterns were recorded to confirm the structure, phase and crystallinity of different samples, as shown in Fig. 3. The diffraction peaks for pure MoS<sub>2</sub> sample (labeled with a “\*” mark) detected at  $2\theta \approx 14.5^\circ, 32.9^\circ$  and  $56.5^\circ$  can be ascribed to the (002), (100) and (106) crystal planes, respectively, as shown in Fig. 3. The hexagonal MoS<sub>2</sub> with  $a = b = 0.316 \text{ nm}$  and  $c = 1.230 \text{ nm}$  is in well agreement with the JCPDS card no. 37-1492. All the XRD peaks for TiO<sub>2</sub> NBs (labeled with “♦” mark) match the standard peak value with the monoclinic B-phase of TiO<sub>2</sub> [5]. From the diffraction pattern of few layer MoS<sub>2</sub> decorated TiO<sub>2</sub>(B) NBs HS, it is noteworthy that the diffraction peak for pure MoS<sub>2</sub> powder at  $\sim 14.5^\circ$  was not detected in case of MoS<sub>2</sub>/TiO<sub>2</sub> HSs. It corresponds to the c-plane of MoS<sub>2</sub> which is composed of Mo atoms coordinated with S atoms to form S-Mo-S sandwich structure. The absence of the peak at  $\sim 14.5^\circ$  in the HSs may be due to the coating with extremely thin few layer MoS<sub>2</sub> nanosheets on the TiO<sub>2</sub> NBs. Additionally, the growth of MoS<sub>2</sub> crystals along the c-axis may be prevented by the TiO<sub>2</sub>(B) NBs when the NBs act as the platform for the nucleation of MoS<sub>2</sub> NFs during the hydrothermal growth.

#### 3.2.2. Raman and FTIR analyses

The crystallinity and phase of TiO<sub>2</sub>, and the number of layers in as-synthesized MoS<sub>2</sub> and MoS<sub>2</sub>/TiO<sub>2</sub> hybrids have been investigated by the micro-Raman analysis and the results are shown in Fig. 4(a)–(c). Each

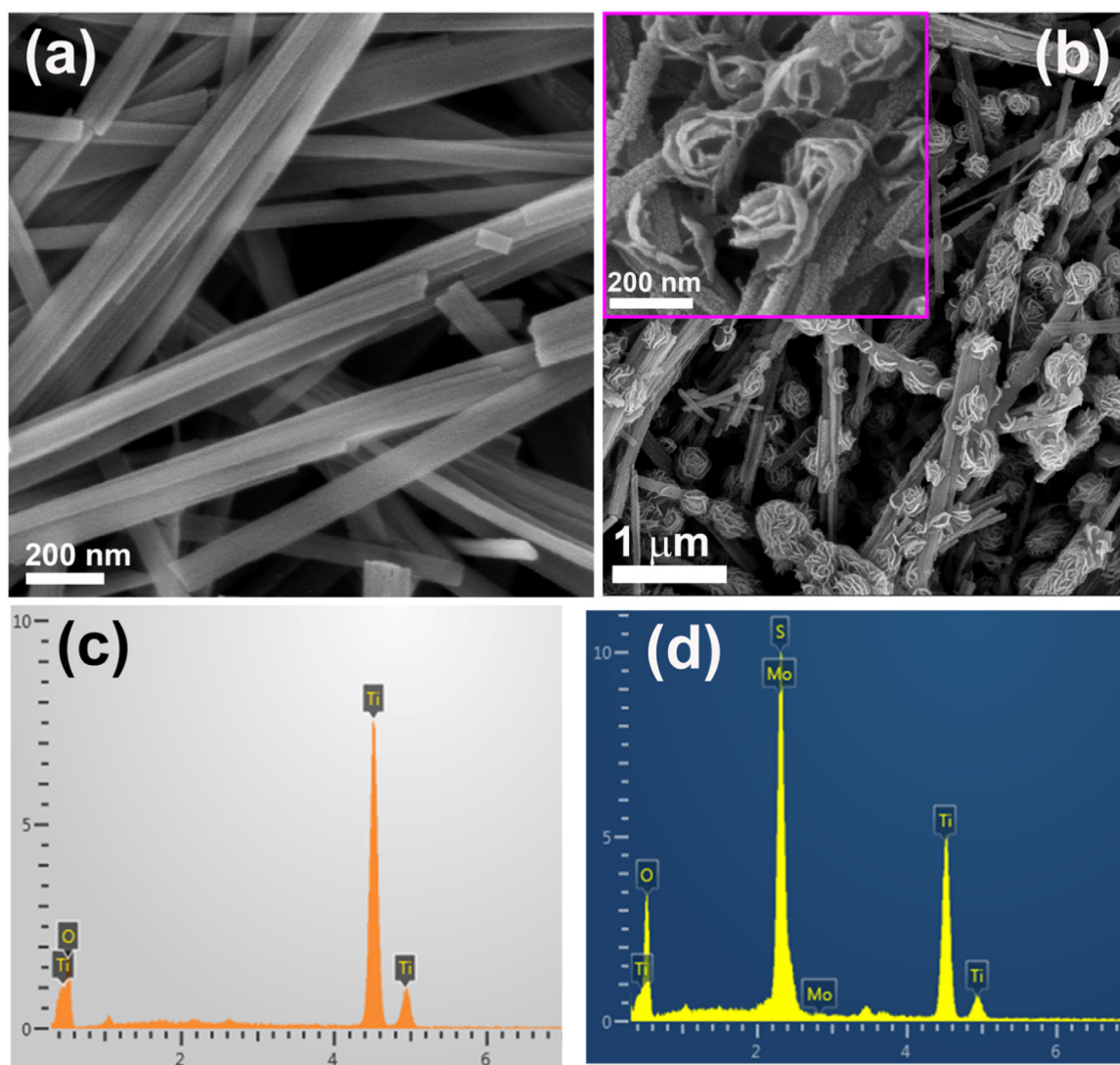


**Fig. 1.** FESEM images of (a) pristine  $\text{TiO}_2$  NBs and (b) uniform decoration of  $\text{MoS}_2$  NFs on  $\text{TiO}_2$  NBs. Inset of (b) shows the enlarged view of  $\text{MoS}_2$  NFs on  $\text{TiO}_2$  NBs. EDX spectra of (c) pristine  $\text{TiO}_2$  NBs and (d)  $\text{MoS}_2/\text{TiO}_2$  HSs, respectively.

Raman peak of the pristine  $\text{TiO}_2$  is assigned to the pure B-phase  $\text{TiO}_2$ , as shown in Fig. 4(a), while that of pure  $\text{MoS}_2$  nanosheets (Fig. 4(b)) exhibits two active modes observed at  $379.7\text{ cm}^{-1}$  and  $404.8\text{ cm}^{-1}$ , which can be assigned to  $E_{2g}^1$  and  $A_{1g}$  modes, respectively. However, in the  $\text{MoS}_2/\text{TiO}_2$  HS (Fig. 4(c)), these Raman modes are observed at  $380.1\text{ cm}^{-1}$  and  $402.4\text{ cm}^{-1}$ , respectively [2,42]. The former peak ( $E_{2g}^1$ ) corresponds to the in-plane vibrations and the later one ( $A_{1g}$ ) to the vertical-plane vibrations in the Mo-S bond of  $\text{MoS}_2$  [43]. It is noteworthy that both the Raman modes of  $\text{MoS}_2$  are shifted in HS sample, which may be interpreted as follows:  $E_{2g}^1$  peak is blue shifted by  $0.4\text{ cm}^{-1}$ , while  $A_{1g}$  peak suffers a huge red shift by  $2.4\text{ cm}^{-1}$ , which may be due to the compressive and tensile strain, respectively in  $\text{MoS}_2$  lattice because of the formation of heterojunction with the  $\text{TiO}_2$ . From Fig. 4(a), it can be observed that the  $B_g$  and  $A_g$  Raman modes for pristine  $\text{TiO}_2$  appear at  $123.1\text{ cm}^{-1}$  and  $146.7\text{ cm}^{-1}$ , respectively which are found to be blue shifted after its decoration with layered  $\text{MoS}_2$  NFs. Thus, in  $\text{MoS}_2/\text{TiO}_2$  HS, the  $B_g$  and  $A_g$  peaks are observed at  $126.3\text{ cm}^{-1}$  and  $153.5\text{ cm}^{-1}$ , respectively as shown in Fig. 4(c), which may be due to the compressive strain induced in the  $\text{TiO}_2$  lattice originating from the nonstoichiometric oxygen vacancy defects, further confirmed by XPS analysis.

The FTIR measurement was carried out in transmission mode to investigate the vibration modes in the crystal lattice of pristine  $\text{TiO}_2$ ,

$\text{MoS}_2$  as well as the HS sample. As shown in Fig. 4(d), for pristine  $\text{TiO}_2$  NBs, the vibration modes at  $477$ ,  $805$  and  $960\text{ cm}^{-1}$  are assigned to the pure  $\text{TiO}_2(\text{B})$  phase. The vibration modes observed at  $477$  and  $960\text{ cm}^{-1}$  are due to the O-Ti-O bending and Ti-O stretching vibrations, respectively, while  $805\text{ cm}^{-1}$  may be assigned to the O-Ti-O bending and Ti-O stretching vibrations. For pristine  $\text{MoS}_2$ , the vibration mode at  $615\text{ cm}^{-1}$  is assigned to Mo-S vibration, while that at  $1120\text{ cm}^{-1}$  may be S-O (sulfide oxide) asymmetric stretching. All the characteristic vibration modes are present in the  $\text{MoS}_2/\text{TiO}_2$  HS without any major shift except with very low S-O vibration mode which clearly implies that the HS contains very less amount of oxidized  $\text{MoS}_2$ . The absorption peaks around  $1650$  and  $3200\text{ cm}^{-1}$  are due to the stretching vibrations of the O-H bonds, assigned to the adsorbed atmospheric water on the surface of the catalysts.

### 3.2.3. XPS analysis

Surface defects present in  $\text{TiO}_2$  NBs and the HS samples were confirmed by investigating the Ti 2p XPS spectra, as shown in Fig. 5(a). The Ti 2p core level XPS spectra were deconvoluted by Gaussian fittings to determine the double peak features of Ti  $2p_{3/2}$  and Ti  $2p_{1/2}$ . The perfect fit for two peaks corresponding to the binding energies at  $458.8$  and  $464.5\text{ eV}$  can be attributed to Ti  $2p_{3/2}$  and Ti  $2p_{1/2}$  core levels of  $\text{Ti}^{4+}$  cations, respectively, confirming the formation of  $\text{TiO}_2$ . Two additional

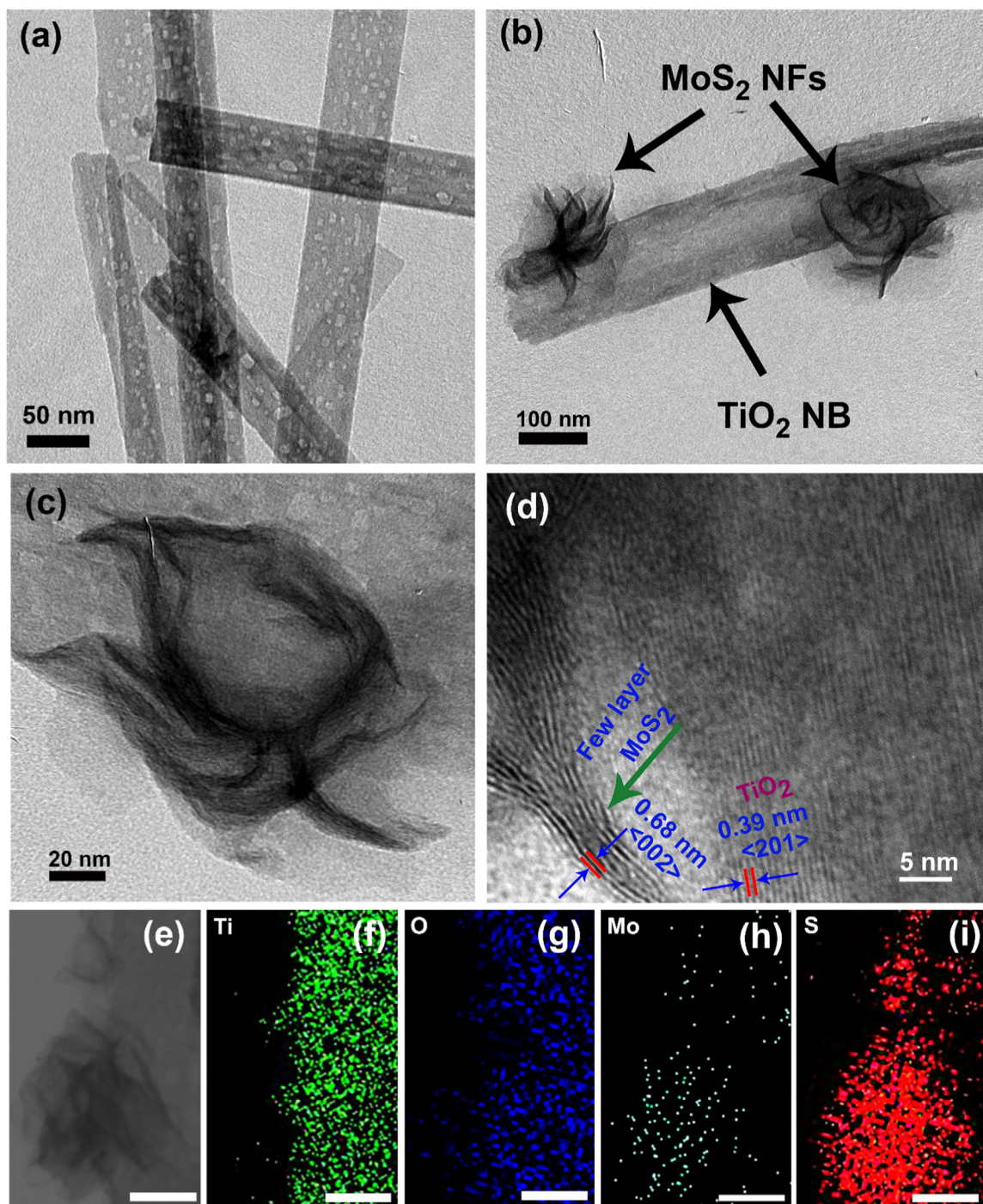


**Fig. 2.** TEM images of (a) nanoporous TiO<sub>2</sub> NBs, (b) MoS<sub>2</sub> NFs on TiO<sub>2</sub> NBs, (c) enlarged view of MoS<sub>2</sub>/TiO<sub>2</sub>(B) hybrid. (d) HRTEM lattice fringe pattern showing the simultaneous presence of TiO<sub>2</sub> and MoS<sub>2</sub>. (e) STEM image of MoS<sub>2</sub>/TiO<sub>2</sub> HS, (f-i) elemental map of Ti, O, Mo and S, respectively. Scale bar is 20 nm in each case.

Gaussian peaks centered at 456.7 eV and 461.0 eV were detected with relative percentage of 4.9% for TiO<sub>2</sub> NBs, which can be attributed to Ti<sup>+3</sup> valence state of Ti 2p<sub>3/2</sub> and Ti 2p<sub>1/2</sub>, respectively. Santara et al. [44] demonstrated that with the loss of an O atom a vacancy cavity (V<sub>O</sub>) is created in the TiO<sub>2</sub> lattice with an electron pair trapped in the vacancy cavity which gives rise to an F center (V<sub>O</sub> + 2e<sup>-</sup> → F). Afterwards, one of the trapped electrons in F center tends to occupy the neighboring Ti<sup>4+</sup> ion and forms Ti<sup>3+</sup> center and F<sup>+</sup> center (F + Ti<sup>4+</sup> → F<sup>+</sup> + Ti<sup>3+</sup>). Thus, both the Ti<sup>3+</sup> center and F<sup>+</sup> center (single electron trapped oxygen vacancy) are formed because of the absence of an oxygen atom, which confirms the presence of nonstoichiometric O<sub>x</sub>

defects in TiO<sub>2</sub>(B) NBs [5]. It is noteworthy that the relative percentage of Ti<sup>3+</sup> increases after the formation of HS with few-layer MoS<sub>2</sub> NFs, which confirms an enhancement in the oxygen vacancy concentration, as confirmed by the Raman analysis. Fig. 5(b) exhibits the Mo 3d core level XPS spectra of MoS<sub>2</sub>/TiO<sub>2</sub> NBs HS. As shown in Fig. 5(b), the strongest Mo 3d doublet peaks for MoS<sub>2</sub>/TiO<sub>2</sub> HS detected at 229.2 eV (3d<sub>5/2</sub>) and 232.5 eV (3d<sub>3/2</sub>), respectively correspond to the 4+ oxidation state confirming the formation of MoS<sub>2</sub>. Shoulder peaks at both the lower and higher binding energies have been observed. The lower energy shoulder peak detected at 226.4 eV can be attributed to the S 2s state and the higher energy shoulder peak detected at 235.7 eV arises

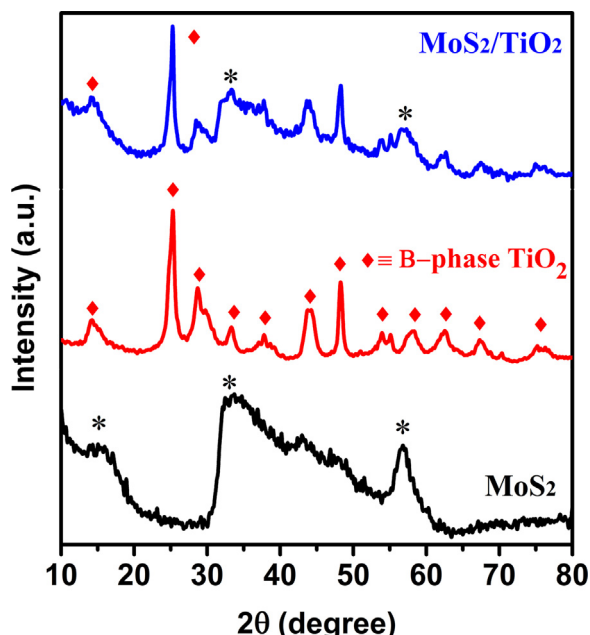


Fig. 3. XRD pattern of few layer MoS<sub>2</sub> NFs, TiO<sub>2</sub>(B) NBs, and MoS<sub>2</sub>/TiO<sub>2</sub> HSs. The curves are vertically shifted for clarity of presentation.

from the 6 + oxidation state of Mo, probably due to the formation of MoO<sub>3</sub> during the hydrothermal growth and post synthesis exposure to air. Fig. 5(c) exhibits the XPS core level spectra of S with two spin-orbit doublets for MoS<sub>2</sub>/TiO<sub>2</sub> NBs HS. The characteristic peaks corresponding to S 2p<sub>3/2</sub> and S 2p<sub>1/2</sub> orbitals of divalent sulfide ions (S<sup>2-</sup>) in MoS<sub>2</sub> are located at 161.9 eV and 163.1 eV, respectively, confirming the formation of MoS<sub>2</sub> in MoS<sub>2</sub>/TiO<sub>2</sub> HS as shown in Fig. 5(c). Besides, an additional set of S doublets have been detected at 163.6 eV and 164.7 eV, suggesting the presence of amorphous sulfur in the system. Fig. 5(d) displays the O 1s spectra of TiO<sub>2</sub> and MoS<sub>2</sub>/TiO<sub>2</sub>. The spectrum corresponding to bare TiO<sub>2</sub> (peak at 530.2 eV) possesses a long tail towards the higher energy region making the spectra asymmetric in nature. In addition, MoS<sub>2</sub>/TiO<sub>2</sub> NBs HS exhibit exceptionally broad O 1s spectrum with peak position 531.3 eV implying the presence of much more defects or contamination on HS surface. The broad and blue shifted spectrum implies the enhanced oxygen vacancy and adsorbed hydroxyl groups in MoS<sub>2</sub>/TiO<sub>2</sub> HSs. These exceptionally high defect states may serve as shallow donors and enhance the charge transfer at the multiple interfaces, which in turn improves the overall dye degradation

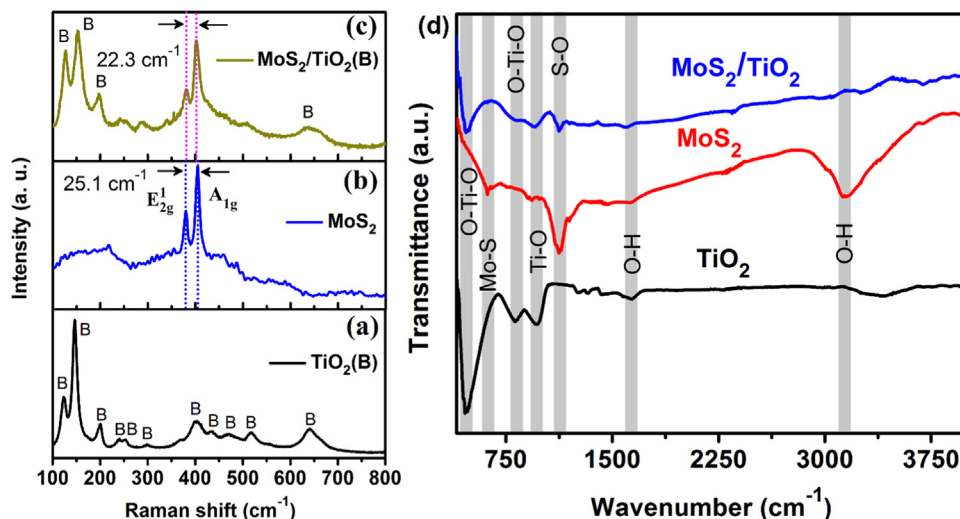


Fig. 4. Raman spectra of (a) pristine TiO<sub>2</sub> NBs, (b) few layer bare MoS<sub>2</sub> NFs, and (c) MoS<sub>2</sub> NFs decorated TiO<sub>2</sub>(B) NBs HS. The vertical dotted lines show the E<sub>2g</sub><sup>1</sup> and A<sub>1g</sub> peaks for layered MoS<sub>2</sub>. (d) Comparison of the FTIR transmittance spectra for TiO<sub>2</sub>, MoS<sub>2</sub> and MoS<sub>2</sub>/TiO<sub>2</sub> showing different vibrational modes. The gray vertical boxes indicate the position of the characteristic modes of TiO<sub>2</sub> and MoS<sub>2</sub>.

efficiency as well as photocatalytic water splitting under solar light, as discussed later.

### 3.3. Brunauer–Emmett–Teller (BET) surface area analysis

In order to investigate the specific surface area and porosity of pristine TiO<sub>2</sub>(B) NBs and its HSs with few-layer MoS<sub>2</sub> NFs, surface area of the samples has been measured by BET process. In Fig. 6(a), the N<sub>2</sub> adsorption-desorption isotherms of TiO<sub>2</sub>(B) NBs and MoS<sub>2</sub>/TiO<sub>2</sub>(B) HSs have been shown. The BET specific surface area of TiO<sub>2</sub>(B) NBs and MoS<sub>2</sub>/TiO<sub>2</sub>(B) HS were determined to be 51.3 m<sup>2</sup>/gm and 47.6 m<sup>2</sup>/gm, respectively. Thus, after loading of MoS<sub>2</sub> NFs on TiO<sub>2</sub>(B), the surface area is reduced marginally as the pores on the TiO<sub>2</sub> NBs are occupied with the MoS<sub>2</sub> nanosheets. Fig. 6(b),(c) shows the Barrett–Joyner–Halenda (BJH) pore size distribution profile of pristine TiO<sub>2</sub>(B) and MoS<sub>2</sub>/TiO<sub>2</sub>(B) HS. Average pore diameter has been estimated from the distribution profile and calculated to be 1.9 nm for TiO<sub>2</sub>(B) NBs and 3.7 nm for MoS<sub>2</sub>/TiO<sub>2</sub>(B) HS. Thus, it can be noted from the Fig. 6(b),(c) that the larger size pores on TiO<sub>2</sub> surface has been passivated by the MoS<sub>2</sub> NFs, while smaller size pore density is increasing confirming the mesoporous nature of MoS<sub>2</sub> NFs.

### 3.4. Optical analysis

#### 3.4.1. UV–Vis absorption study

To measure the optical response of TiO<sub>2</sub>(B) NBs and MoS<sub>2</sub>/TiO<sub>2</sub>(B) HSs, the diffuse reflectance spectra (DRS) of the powdered samples were recorded. The absorbance of a material is correlated with the diffuse reflectance (R<sub>∞</sub>) by the Kubelka-Munk (K-M) function, F(R<sub>∞</sub>), given by

$$F(R_{\infty}) = \frac{(1-R_{\infty})^2}{2R_{\infty}} = \frac{k}{S} = \frac{2.303 \cdot A}{S \cdot d}$$

where, k and S represent the absorption and scattering coefficients, while A and d represent absorbance and thickness of the absorbing layer, respectively. The scattering coefficient, S, was introduced as a semi-empirical parameter in the theoretical description of diffuse reflection to account the internal scattering processes, which is dominated by particle size and refractive index of the sample. If the scattering coefficient does not vary significantly with the wavelength, the K-M function is approximately proportional to the absorption coefficient or absorbance of the sample. Fig. 7(a) shows the plot of the K-M function of different samples depicting the K-M plots and Fig. 7(b) shows the corresponding (F(R)hv)<sup>1/2</sup> vs. hv plot for the calculation of effective band gap (indirect) of the HSs. Extrapolation of the linear

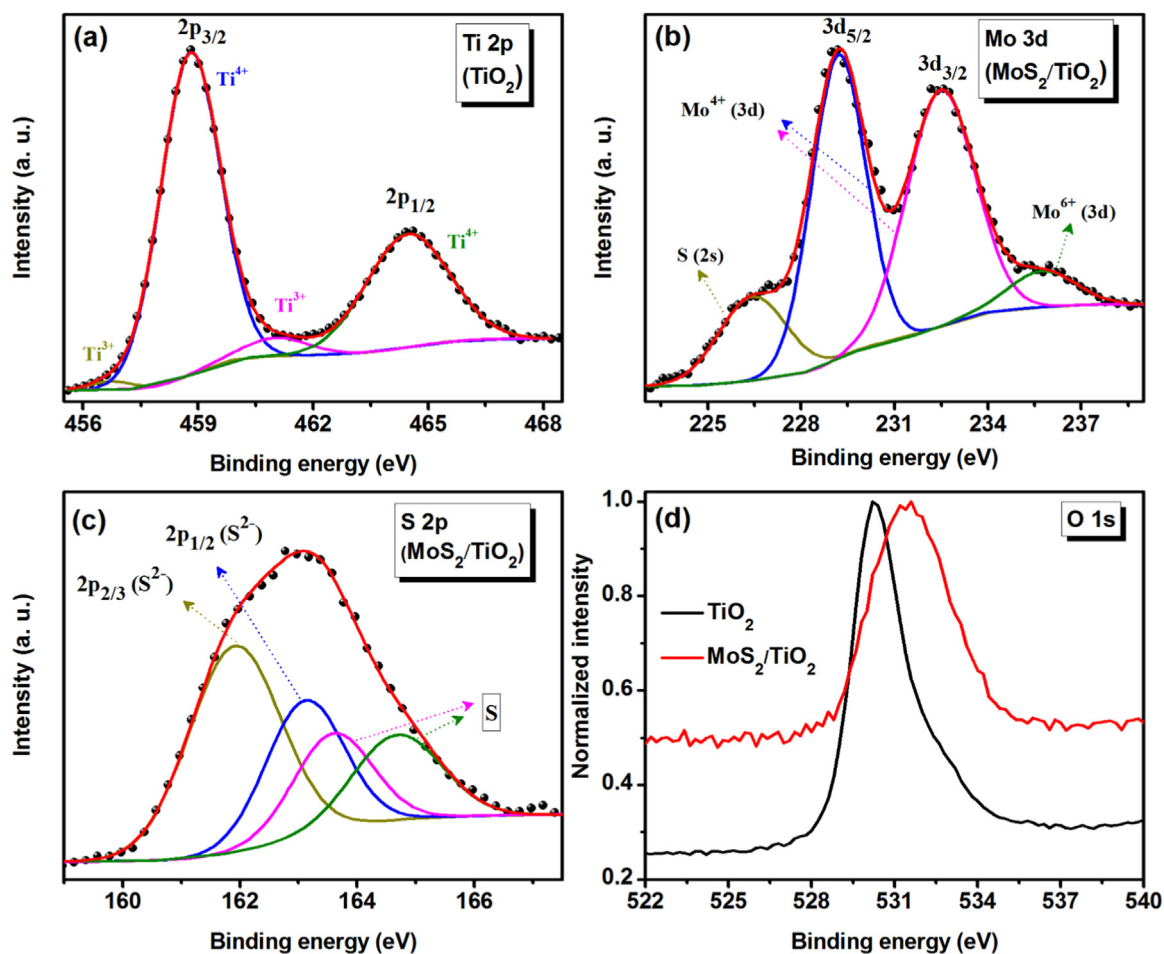


Fig. 5. XPS core level spectra for (a) Ti 2p in TiO<sub>2</sub> NBs, (b) Mo 3d in MoS<sub>2</sub>/TiO<sub>2</sub> HS, (c) S 2p in MoS<sub>2</sub>/TiO<sub>2</sub>, fitted with the Shirley baseline. The symbols represent the experimental data and the solid lines correspond to the Gaussian fits. Identity of each fitted peak is denoted with corresponding charge states in the respective cases. (d) O 1s core level XPS spectra of pure TiO<sub>2</sub> NBs and MoS<sub>2</sub>/TiO<sub>2</sub> NBs HS.

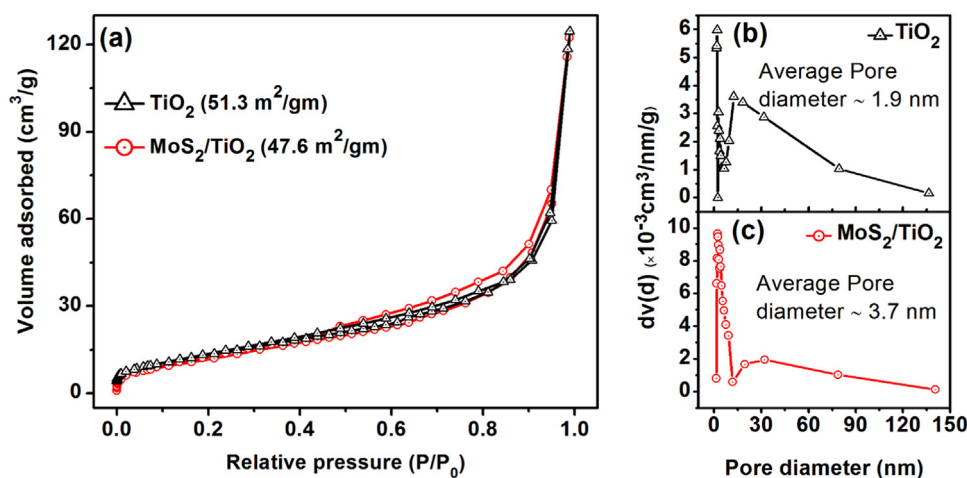


Fig. 6. (a) N<sub>2</sub> adsorption-desorption isotherms for TiO<sub>2</sub>(B) NBs and MoS<sub>2</sub>/TiO<sub>2</sub>(B) HS. Pore size distribution using BJH method for (b) TiO<sub>2</sub>(B) NBs and (c) MoS<sub>2</sub>/TiO<sub>2</sub>(B) HS.

portion at  $(F(R)h\nu)^{1/2} = 0$  provides the effective indirect band gap of the catalysts. The pure TiO<sub>2</sub>(B) NBs exhibit a sharp fundamental absorption edge at ~372 nm that can be assigned to its intrinsic band gap absorption. Pure MoS<sub>2</sub> NFs show a broad absorption band having a peak at ~670 nm with a large blue shift compared to its bulk counterpart having an absorption edge at ~1010 nm (indirect band gap ~1.23 eV).

This may be attributed to the strong quantum confinement effect of the thin and layered MoS<sub>2</sub> nanosheets making the MoS<sub>2</sub> an effective candidate for the solar light driven photocatalysis [45]. After the incorporation of few layer MoS<sub>2</sub> NFs on TiO<sub>2</sub> NBs, the visible to NIR absorption intensity was increased significantly with a broad absorption peak at ~810 nm as compared to the pristine TiO<sub>2</sub> NBs. Interestingly,

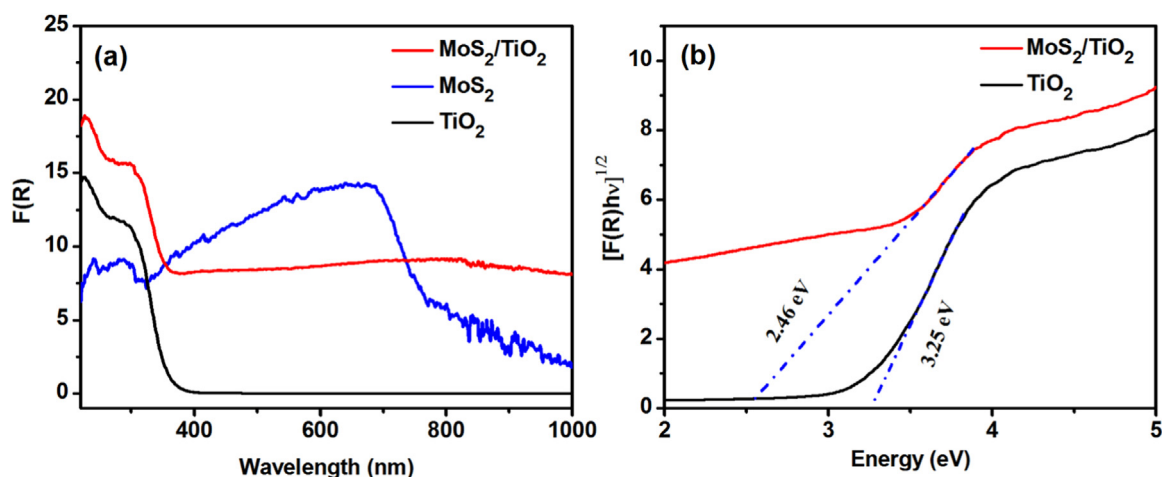


Fig. 7. (a) Kubelka–Munk plot,  $F(R)$  of different catalysts derived from the diffuse reflectance spectra. (b) The corresponding Tauc plot considering the indirect band gap nature of  $\text{TiO}_2$  and its HS with  $\text{MoS}_2$ . The effective band gaps of the respective samples are estimated by the intercept on the x-axis (extrapolated lines).

the effective indirect band gap of  $\text{TiO}_2(\text{B})$  NBs is found to be reduced from 3.25 eV to 2.46 eV after its decoration with the few-layer  $\text{MoS}_2$  NFs, which eventually assist to achieve the enhanced solar light photodegradation of organic dye (RhB) as well as photoelectrocatalytic hydrogen evolution by water splitting. After the formation of HS with  $\text{MoS}_2$  NFs, the efficient band bending at the interface arises from the strong coupling between the porous  $\text{TiO}_2$  and  $\text{MoS}_2$  layers. Thus, the HSs are expected to be extremely sensitive to the visible light and would be beneficial for the efficient solar light driven photocatalytic hydrogen evolution.

### 3.5. Photocatalytic degradation of RhB

The visible light photocatalytic activity of  $\text{TiO}_2$  NBs and its heterojunctions with few layer  $\text{MoS}_2$  NFs was evaluated by measuring the degradation of RhB as a reference dye under the visible light irradiation as shown in Fig. 8. Prior to the illumination, each catalyst was dispersed in the dye solution (RhB) and subjected to a vigorous magnetic stirring for 40 min under dark condition. After 40 min of stirring under dark,  $\text{MoS}_2/\text{TiO}_2$  HS shows  $\sim 66\%$  of adsorption of dye, RhB whereas pristine  $\text{TiO}_2$  NBs show only  $\sim 9\%$  of adsorption. Thus, it is observed that the

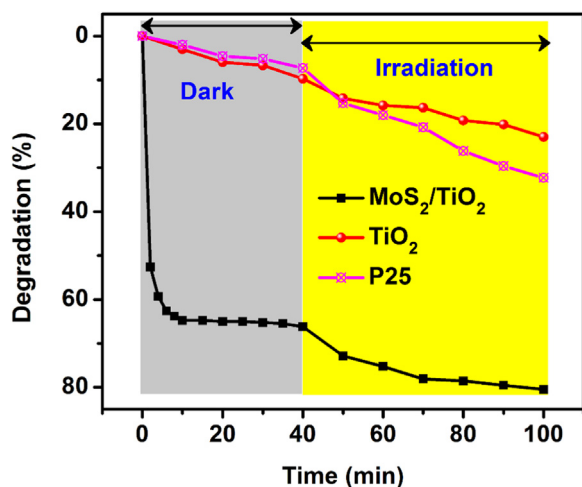


Fig. 8. Comparison of the photocatalytic degradation profiles of RhB with the presence of different catalyst samples under visible light irradiation. The gray region implies the dark condition and the yellow region implies the irradiation zone. (For interpretation of the references to color in this figure legend, the reader is referred to the web version of this article.)

few-layer  $\text{MoS}_2$  NFs decorated porous  $\text{TiO}_2$  NBs exhibit extremely high adsorption efficiency under dark. Further, it can be noted that the degradation of the dye after 60 min of irradiation is calculated to be  $\sim 80\%$  for  $\text{MoS}_2/\text{TiO}_2$  HS and only  $\sim 23\%$  for  $\text{TiO}_2$  NBs. For a better comparison, the degradation study was performed with commercial P25 photocatalyst under identical conditions. It is observed that after 40 min of stirring under dark, only  $\sim 7\%$  of dye is adsorbed on its surface and after 60 min of visible light irradiation only  $\sim 32\%$  of dye is degraded. Thus, it can be concluded that the HS photocatalyst ( $\text{MoS}_2/\text{TiO}_2$ ) is superior in performance as compared to the commercial P25 under visible light.

The possible mechanism behind the high adsorption and photocatalytic degradation of RhB by  $\text{MoS}_2/\text{TiO}_2$  HSs compared to the pristine  $\text{TiO}_2$  NBs is explained follows. It has been reported that the few layer  $\text{MoS}_2$  nanosheets with large surface area and pore diameter show very good adsorption of dye with extremely rapid rate [46]. Here, highly efficient few layer  $\text{MoS}_2$  nanosheets integrated with porous  $\text{TiO}_2$  NBs can adsorb the dye with very fast rate. Additionally, the Raman and XPS analyses reveal that the HSs are highly defective in nature. The defect lies mainly on surfaces and nonstoichiometric oxygen vacancy type in nature. Thus, the HSs ( $\text{MoS}_2/\text{TiO}_2$ ) from its surface act as anionic in nature. When this highly anionic catalyst is added in the cationic dye solution (aqueous RhB solution), the freely suspended dye molecules in the solution feel Coulombic attraction towards the catalyst particles and get attached to them with very fast rate. Additionally,  $\text{MoS}_2/\text{TiO}_2$  heterojunction is staggered type in nature (type-II), as shown in Fig. 9(d), which accelerates the photogenerated charge transfer at their interfaces while irradiating with visible light by reducing their recombination probability [47]. Thus, the migrated electrons and holes create highly active super oxide radicals and hydroxyl radicals. These eventually enhances the dye degradation rate than its individual components [1,5].

### 3.6. Hydrogen evolution reaction (HER) studies

The visible light HER performance of various catalysts, such as  $\text{TiO}_2$  and  $\text{MoS}_2/\text{TiO}_2$  as working electrodes made on glassy carbon disk were investigated using three electrode linear sweep voltammetry (LSV) method. For a better comparison, all the measurements have been repeated under dark condition as well. The electrochemical HER activities (in 0.5 M  $\text{H}_2\text{SO}_4$ ) of various catalysts under dark and light (wavelength range 370–730 nm) are shown in Fig. 9(a) and the corresponding Tafel slopes, calculated from the linear fit of the on-set potential at which HER starts, are shown in Fig. 9(b). As shown in Fig. 9(a), the HER reaction for  $\text{TiO}_2$  NBs starts at an overpotential of  $\approx -623$  mV and

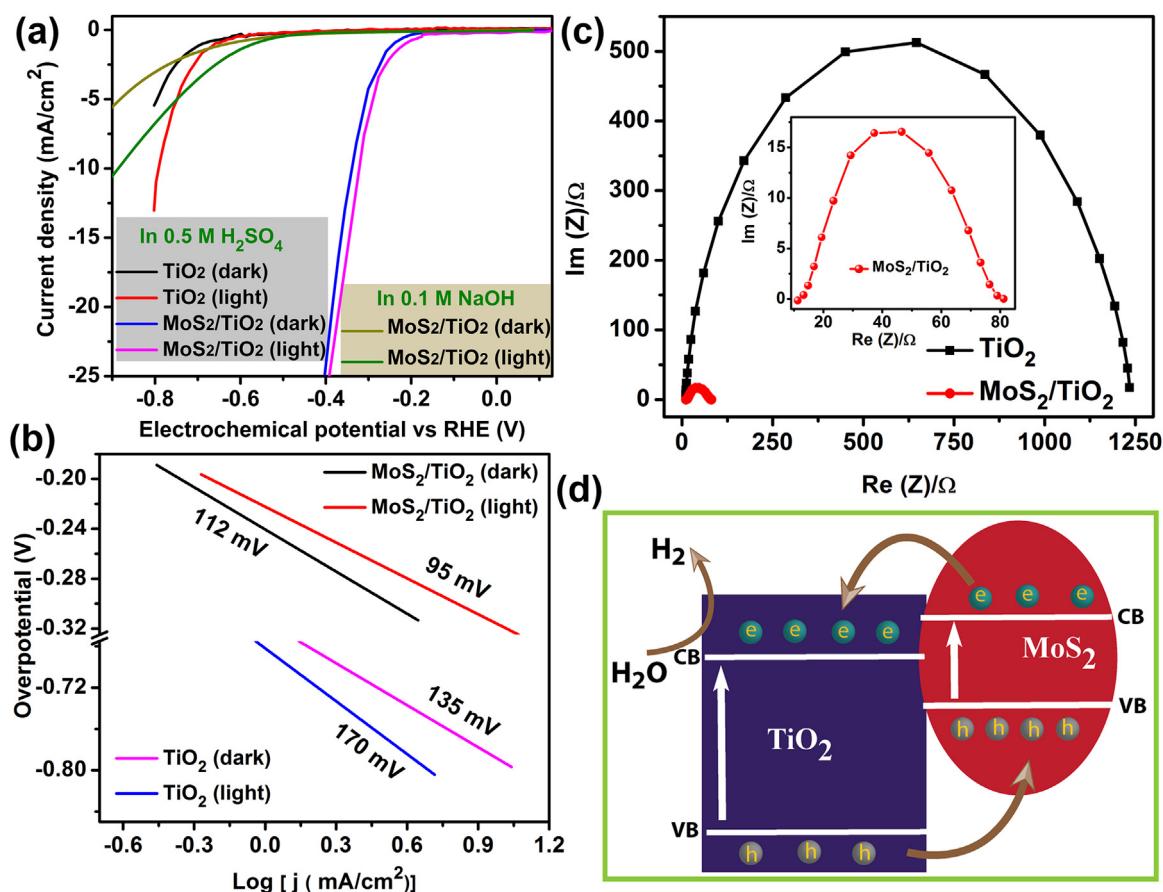


**Fig. 9.** (a) Polarization curves of hydrogen evolution reaction (HER) in dark and light conditions for  $\text{TiO}_2(\text{B})$  NBs and  $\text{MoS}_2/\text{TiO}_2(\text{B})$  NBs HS, the Tafel slope of respective samples is shown in (b). Polarization curve for  $\text{MoS}_2/\text{TiO}_2(\text{B})$  HS was recorded in two different electrolyte solution, 0.5 M  $\text{H}_2\text{SO}_4$  and 0.1 M NaOH. (c) Nyquist plots of  $\text{TiO}_2(\text{B})$  NBs and  $\text{MoS}_2/\text{TiO}_2(\text{B})$  NBs HS. Inset shows a magnified view of the  $\text{MoS}_2/\text{TiO}_2(\text{B})$  NBs HS. (d) Schematic illustration of charge transfer process at the interface and the mechanism of enhanced visible light photoelectrocatalytic activity.

$\approx -616$  mV (versus RHE) under dark and light, respectively, above which the current increases drastically. In spite of very low overall current density, more than two fold enhancement in the current density was observed at  $-800$  mV after illuminating the electrode as compared to the dark case. Interestingly, the uniform decoration with few-layer  $\text{MoS}_2$  NFs on the  $\text{TiO}_2$  NBs surface brought down the overpotential to  $\approx -215$  mV in dark, which further diminishes to  $\approx -180$  mV after irradiating with visible light with a drastic enhancement in the current density as compared to the bare  $\text{TiO}_2$  NBs. In this system ( $\text{MoS}_2/\text{TiO}_2$  NBs HS) the current density reaches to  $10 \text{ mA/cm}^2$  with the potential  $-340$  mV in dark, which shifts to  $-320$  mV after 20 min of light irradiation. Thus, it can be concluded that more number of carriers are being generated in presence of light than the dark. When we carried out HER at pH 12, we noticed that the HER activity of  $\text{MoS}_2/\text{TiO}_2$  deteriorated dramatically, as shown in Fig. 9(a). The overpotential shows a large shift to  $\sim -1.025$  V under dark and  $\sim -886$  mV under light compared to its low pH electrolyte. Thus, it can be argued that the standard pH value of the electrolyte (0.5 M  $\text{H}_2\text{SO}_4$ ) is much better than the higher pH electrolyte in order to get superior HER activity.

In principle, a lower Tafel slope signifies a lower applied overpotential required to generate a sufficient current, which acts as determining step towards the kinetics of HER reaction. Tafel slope of all the samples in both dark and light are shown in Fig. 9(b) and tabulated in Table 1. From Fig. 9(b) it is evident that in each catalyst, the Tafel slope decreases after the illumination of light compared to their respective dark values, which eventually confirms the acceleration in the charge transfer rate with the irradiation. Pristine  $\text{TiO}_2$  NBs exhibit very high Tafel slope under dark,  $170 \text{ mV/dec}$ , which reduces to  $135 \text{ mV/dec}$

**Table 1**

Sample specification, effective band gap, oxygen vacancy, hydroxyl group, over-potential and Tafel slope for different samples.

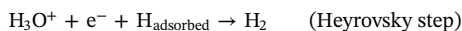
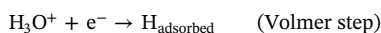
Sample	Effective band gap (eV)	$\text{O}_v$ % in O 1s XPS spectrum	$\text{O}_H$ % in O 1s XPS spectrum	Over-potential [mV RHE]		Tafel slope (mV)/dec	
				dark	light	dark	light
$\text{TiO}_2(\text{B})$	3.25	22.2	18.4	-880	-792	170	135
$\text{MoS}_2/\text{TiO}_2(\text{B})$	2.46	46.1	32.7	-340	-320	112	95

dec after irradiating with visible light. The  $\text{MoS}_2/\text{TiO}_2$  NBs HS exhibits much lower Tafel slope,  $112 \text{ mV/dec}$  under dark, which reduces drastically to  $95 \text{ mV/dec}$  after 20 min of irradiation. As discussed in the literatures, Tafel slope with values  $\sim 120 \text{ mV/decade}$ ,  $\sim 40 \text{ mV/decade}$  and  $\sim 30 \text{ mV/decade}$  follow Volmer, Heyrovsky and Tafel reaction mechanisms, respectively [48–52]. In our case, the Tafel slope of the HS photocatalyst ( $\text{MoS}_2/\text{TiO}_2$ ) falls between the Volmer mechanism and the Heyrovsky mechanism indicating the reaction mechanism as Volmer–Heyrovsky type [53]. As expected from the extremely reduced Tafel slope, the  $\text{MoS}_2/\text{TiO}_2$  HSs behave as high performance catalyst towards HER reaction. The above enhanced HER performance of  $\text{MoS}_2/\text{TiO}_2$  can be attributed to the efficient charge transport and favorable HER kinetics at the interface of HS components.

Electrochemical impedance spectroscopy (EIS) is a powerful technique to characterize interface reactions and electrode kinetics in HER [54]. Fig. 9(c) shows the Nyquist plots of all the samples corresponding to their EIS response. The inset shows a magnified view of the plot for the HS sample, which shows very low charge transfer resistance ( $R_{CT}$ ).

The  $R_{CT}$  values have been calculated for all the samples estimated from the Randles circuit, as discussed by Biroju et al. [55]. The  $R_{CT}$  is calculated to be very high for pristine  $TiO_2$  NBs (1.2 k $\Omega$ ), which is reduced greatly after its integration with few layer  $MoS_2$  NFs and found to be 80  $\Omega$ . The  $R_{CT}$  is directly related to the kinetics of electrocatalysis and a lower value signifies a rapid charge transfer corresponding to faster reaction rate. Catalytically active edge sites of  $MoS_2$  providing a fast electron transfer between the  $MoS_2$  and  $TiO_2$  results in a superior HER kinetics.

The following factors may be responsible for the enhancement of HER activity of  $TiO_2$  NBs incorporated with few-layer  $MoS_2$  NFs. The drastic enhancement in the current density after the formation of heterojunction between  $MoS_2$  and  $TiO_2$  indicates increase in the catalytically active surface area compared to bare  $TiO_2$  NBs. Additionally, the modification by  $H_2SO_4$  decreases the work function of  $TiO_2$ , which changes its conduction band offset [56]. Thus, the charge transfer process becomes faster through the type-II heterojunction of  $TiO_2$  and  $MoS_2$ , which results in improved HER activity (see Fig. 9(d)). The structurally defective  $TiO_2$  surface ( $O_v$  rich, as confirmed from XPS analysis) allows closer bonding between  $MoS_2$  and  $TiO_2$  and it may introduce more defect edges in the  $MoS_2$  NFs. The morphology of the as-grown  $MoS_2$  NFs on the  $TiO_2$  NBs confirms its edge-rich nature, many obvious ripples, dislocations, and corrugations resulting in more unsaturated sulfur edge sites enhancing the overall HER activity. UV–visible absorbance spectra confirm a broad visible–NIR light absorption in the wavelength range of 400–1000 nm. Thus, the dramatic improvement in the HER activity under visible light is partly due to the improved absorption in the entire UV–Vis–NIR region. The incorporated impurities in  $TiO_2$  lattice increase greatly after the decoration of  $MoS_2$  NFs, as confirmed from XPS analysis (see Fig. 5(d)). As the Volmer–Heyrovsky HER mechanism is operative in our HS catalysts, rate limiting electrochemical desorption step involves the formation of hydrogen gas from the adsorbed atomic hydrogen at the working electrode, which follows the pathways:



#### 4. Conclusion

Herein,  $MoS_2/TiO_2$  NBs HS was successfully prepared via a hydrothermal reaction considering porous  $TiO_2$  NBs as a template. Uniform decoration of rose-like  $MoS_2$  NFs over the surface of porous  $TiO_2$  NBs has been evidenced by the FESEM and FETEM analyses. The formation of  $O_v$  rich  $MoS_2/TiO_2$  NBs HS and a broad visible to NIR optical absorption have been evidenced by the XPS and UV–vis absorption spectra, respectively. The HER activity of  $TiO_2$  NBs is greatly enhanced after the decoration of  $MoS_2$  NFs. The overpotential is observed to be decreased to –320 mV from –792 mV after the decoration of few-layer  $MoS_2$  NFs on  $TiO_2$  under visible light irradiation and the corresponding Tafel slope reduced to 95 mV/dec from 135 mV/dec. The  $MoS_2/TiO_2$  HSs exhibit a major enhancement in HER activity as supported by the EIS spectra, which revealed that the charge transfer resistance of  $TiO_2(B)$  NBs decreases from 1200  $\Omega$  to 80  $\Omega$  after the incorporation of  $MoS_2$  NFs. Additionally, high adsorption and enhanced photocatalytic decomposition of RhB under visible light are demonstrated for the hybrid. Further enhancement of the PEC performance may be expected by decorating of catalyst metal nanoparticles over the hybrid structure, for which optimization of the growth process is essential. Nevertheless, this study demonstrates that edge-exposed few-layer  $MoS_2$  NFs decorated on porous  $TiO_2$  NBs HS is a promising candidate for the application of environmental remediation as well as hydrogen generation by water splitting.

#### Acknowledgements

We acknowledge the financial support from MEITY (Grant No. 5(9)/2012-NANO(VOL-II)) for carrying out part of this work. N. Sreekanth acknowledges postdoctoral fellowship from SERB-NPDF (PDF/2016/002763). RKB acknowledges the postdoctoral fellowship from SERB-NPDF (PDF/2016/002642). Central Instruments Facility, I.I.T. Guwahati is acknowledged for providing the Raman, TEM and FESEM facilities. We thank Prof. M. Fujii, Kobe University, Japan for help in the XPS measurement.

#### Appendix A. Supporting information

Supplementary data associated with this article can be found in the online version at <http://dx.doi.org/10.1016/j.solmat.2018.05.056>.

#### References

- [1] W. Zhou, Z. Yin, Y. Du, X. Huang, Z. Zeng, Z. Fan, H. Liu, J. Wang, H. Zhang, Synthesis of few-layer  $MoS_2$  nanosheet-coated  $TiO_2$  nanobelt heterostructures for enhanced photocatalytic activities, *Small* 9 (2013) 140–147.
- [2] H. Li, Y. Wang, G. Chen, Y. Sang, H. Jiang, J. He, X. Li, H. Liu, Few-layered  $MoS_2$  nanosheets wrapped ultrafine  $TiO_2$  nanobelts with enhanced photocatalytic property, *Nanoscale* 8 (2016) 6101–6109.
- [3] H.J. Kim, S.H. Lee, A.A. Upadhye, I. Ro, M.I. Tejedor-Tejedor, M.A. Anderson, W.B. Kim, G.W. Huber, Plasmon-enhanced photoelectrochemical water splitting with size-controllable gold nanodot arrays, *ACS Nano* 8 (2014) 10756–10765.
- [4] A. Fujishima, K. Honda, Electrochemical photolysis of water at a semiconductor electrode, *Nature* 238 (1972) 37–38.
- [5] K.K. Paul, R. Ghosh, P.K. Giri, Mechanism of strong visible light photocatalysis by  $Ag_2O$ -nanoparticle-decorated monoclinic  $TiO_2$  (B) porous nanorods, *Nanotechnology* 27 (2016) 315703.
- [6] R. Asahi, T. Morikawa, T. Ohwaki, K. Aoki, Y. Taga, Visible-light photocatalysis in nitrogen-doped titanium oxides, *Science* 293 (2001) 269.
- [7] V. Binas, D. Venieri, D. Kotzias, G. Kiriakidis, Modified  $TiO_2$  based photocatalysts for improved air and health quality, *J. Mater.* 3 (2017) 3–16.
- [8] K.R. Reddy, K. Nakata, T. Ochiai, T. Murakami, D.A. Tryk, A. Fujishima, Facile fabrication and photocatalytic application of Ag nanoparticles- $TiO_2$  nanofiber composites, *J. Nanosci. Nanotechnol.* 11 (2011) 3692–3695.
- [9] K.R. Reddy, M. Hassan, V.G. Gomes, Hybrid nanostructures based on titanium dioxide for enhanced photocatalysis, *Appl. Catal. A: Gen.* 489 (2015) 1–16.
- [10] J. Shuai, L. Ingo, L. Katharina, M.-E. Rafael, C. Daniel, Nanofibrous photocatalysts from electrospun nanocapsules, *Nanotechnology* 28 (2017) 405601.
- [11] K.R. Reddy, K. Nakata, T. Ochiai, T. Murakami, D.A. Tryk, A. Fujishima, Nanofibrous  $TiO_2$ -core/conjugated polymer-sheath composites: synthesis, structural properties and photocatalytic activity, *J. Nanosci. Nanotechnol.* 10 (2010) 7951–7957.
- [12] K.R. Reddy, V.G. Gomes, M. Hassan, Carbon functionalized  $TiO_2$  nanofibers for high efficiency photocatalysis, *Mater. Res. Express* 1 (2014) 015012.
- [13] X. Chen, L. Liu, P.Y. Yu, S.S. Mao, Increasing solar absorption for photocatalysis with black hydrogenated titanium dioxide nanocrystals, *Science* 331 (2011) 746–750.
- [14] Y. Gai, J. Li, S.-S. Li, J.-B. Xia, S.-H. Wei, Design of narrow-gap  $TiO_2$ : a passivated codoping approach for enhanced photoelectrochemical activity, *Phys. Rev. Lett.* 102 (2009) 036402.
- [15] W.J. Zhou, Y.H. Leng, D.M. Hou, H.D. Li, L.G. Li, G.Q. Li, H. Liu, S.W. Chen, Phase transformation and enhanced photocatalytic activity of S-doped  $Ag_2O/TiO_2$  heterostructured nanobelts, *Nanoscale* 6 (2014) 4698.
- [16] W. Zhou, H. Liu, J. Wang, D. Liu, G. Du, J. Cui,  $Ag_2O/TiO_2$  nanobelts heterostructure with enhanced ultraviolet and visible photocatalytic activity, *ACS Appl. Mater. Interfaces* 2 (2010) 2385.
- [17] K.K. Paul, P.K. Giri, Role of surface plasmons and hot electrons on the multi-step photocatalytic decay by defect enriched  $Ag@TiO_2$  nanorods under visible light, *J. Phys. Chem. C* 121 (2017) 20016–20030.
- [18] M.-Z. Ge, C.-Y. Cao, S.-H. Li, Y.-X. Tang, L.-N. Wang, N. Qi, J.-Y. Huang, K.-Q. Zhang, S.S. Al-Deyab, Y.-K. Lai, In situ plasmonic Ag nanoparticle anchored  $TiO_2$  nanotube arrays as visible-light-driven photocatalysts for enhanced water splitting, *Nanoscale* 8 (2016) 5226–5234.
- [19] A. Tanaka, A. Ogino, M. Iwaki, K. Hashimoto, A. Ohnuma, F. Amano, B. Ohtani, H. Kominami, Gold–titanium(IV) oxide plasmonic photocatalysts prepared by a colloid-photodeposition method: correlation between physical properties and photocatalytic activities, *Langmuir* 28 (2012) 13105.
- [20] M.A. Khan, L. Sinatra, M. Oufi, O.M. Bakr, H. Idriss, Evidence of plasmonic induced photocatalytic hydrogen production on Pd/ $TiO_2$  upon deposition on thin films of gold, *Catal. Lett.* 147 (2017) 811–820.
- [21] K.R. Reddy, B.C. Sin, C.H. Yoo, W. Park, K.S. Ryu, J.-S. Lee, D. Sohn, Y. Lee, A new one-step synthesis method for coating multi-walled carbon nanotubes with cuprous oxide nanoparticles, *Scr. Mater.* 58 (2008) 1010–1013.
- [22] K.R. Reddy, K.P. Lee, A.I. Gopalan, M.S. Kim, A.M. Showkat, Y.C. Nho, Synthesis of metal (Fe or Pd)/alloy (Fe–Pd)-nanoparticles-embedded multiwall carbon

- nanotube/sulfonated polyaniline composites by  $\gamma$  irradiation, *J. Polym. Sci. Part A: Polym. Chem.* 44 (2006) 3355–3364.
- [23] K.R. Reddy, K.P. Lee, A.I. Gopalan, Self-assembly approach for the synthesis of electro-magnetic functionalized Fe<sub>3</sub>O<sub>4</sub>/polyaniline nanocomposites: effect of dopant on the properties, *Colloids Surf. A: Physicochem. Eng. Asp.* 320 (2008) 49–56.
- [24] X. Deng, C.K. Chan, H. Tüysüz, Spent tea leaf templating of cobalt-based mixed oxide nanocrystals for water oxidation, *ACS Appl. Mater. Interfaces* 8 (2016) 32488–32495.
- [25] M. Hassan, E. Haque, K.R. Reddy, A.I. Minett, J. Chen, V.G. Gomes, Edge-enriched graphene quantum dots for enhanced photo-luminescence and supercapacitance, *Nanoscale* 6 (2014) 11988–11994.
- [26] A.M. Showkat, Y.-P. Zhang, M.-S. Kim, A.I. Gopalan, K.R. Reddy, K.-P. Lee, Analysis of heavy metal toxic ions by adsorption onto amino-functionalized ordered mesoporous silica, *Bull. Korean Chem. Soc.* 28 (2007) 1985–1992.
- [27] K.R. Reddy, K.-P. Lee, A.I. Gopalan, Self-assembly directed synthesis of poly (ortho-luidine)-metal (gold and palladium) composite nanospheres, *J. Nanosci. Nanotechnol.* 7 (2007) 3117–3125.
- [28] Y.P. Zhang, S.H. Lee, K.R. Reddy, A.I. Gopalan, K.P. Lee, Synthesis and characterization of core-shell SiO<sub>2</sub> nanoparticles/poly(3-aminophenylboronic acid) composites, *J. Appl. Polym. Sci.* 104 (2007) 2743–2750.
- [29] F.-X. Xiao, S.-F. Hung, H.B. Tao, J. Miao, H.B. Yang, B. Liu, Spatially branched hierarchical ZnO nanorod-TiO<sub>2</sub> nanotube array heterostructures for versatile photocatalytic and photoelectrocatalytic applications: towards intimate integration of 1D-1D hybrid nanostructures, *Nanoscale* 6 (2014) 14950–14961.
- [30] T. Jiang, C. Jia, L. Zhang, S. He, Y. Sang, H. Li, Y. Li, X. Xu, H. Liu, Gold and gold-palladium alloy nanoparticles on heterostructured TiO<sub>2</sub> nanobelts as plasmonic photocatalysts for benzyl alcohol oxidation, *Nanoscale* 7 (2015) 209–217.
- [31] F. Meng, S.K. Cushing, J. Li, S. Hao, N. Wu, Enhancement of solar hydrogen generation by synergistic interaction of La<sub>2</sub>Ti<sub>2</sub>O<sub>7</sub> photocatalyst with plasmonic gold nanoparticles and reduced graphene oxide nanosheets, *ACS Catalysis* 5 (2015) 1949–1955.
- [32] W.S. Hummers, R.E. Offeman, Preparation of graphitic oxide, *J. Am. Chem. Soc.* 80 (1958) (1339-1339).
- [33] S. Stankovich, D.A. Dikin, G.H.B. Dommett, K.M. Kohlhaas, E.J. Zimney, E.A. Stach, R.D. Piner, S.T. Nguyen, R.S. Ruoff, Graphene-based composite materials, *Nature* 442 (2006) 282–286.
- [34] Z. Yin, S. Sun, T. Salim, S. Wu, X. Huang, Q. He, Y.M. Lam, H. Zhang, organic photovoltaic devices using highly flexible reduced graphene oxide films as transparent electrodes, *ACS Nano* 4 (2010) 5263–5268.
- [35] Y. Li, Y.-L. Li, C.M. Araujo, W. Luo, R. Ahuja, Single-layer MoS<sub>2</sub> as an efficient photocatalyst, *Catal. Sci. Technol.* 3 (2013) 2214–2220.
- [36] D. Wang, Z. Wang, C. Wang, P. Zhou, Z. Wu, Z. Liu, Distorted MoS<sub>2</sub> nanostructures: an efficient catalyst for the electrochemical hydrogen evolution reaction, *Electrochem. Commun.* 34 (2013) 219–222.
- [37] H. Li, K. Yu, C. Li, Z. Tang, B. Guo, X. Lei, H. Fu, Z. Zhu, Charge-transfer induced high efficient hydrogen evolution of MoS<sub>2</sub>/graphene cocatalyst, *Sci. Rep.* 5 (2015) 18730.
- [38] H. Li, C. Tsai, A.L. Koh, L. Cai, A.W. Contryman, A.H. Fragapane, J. Zhao, H.S. Han, H.C. Manoharan, F. Abild-Pedersen, J.K. Nørskov, X. Zheng, Activating and optimizing MoS<sub>2</sub> basal planes for hydrogen evolution through the formation of strained sulphur vacancies, *Nat. Mater.* 15 (2015) 48.
- [39] B. Pourabbas, B. Jamshidi, Preparation of MoS<sub>2</sub> nanoparticles by a modified hydrothermal method and the photo-catalytic activity of MoS<sub>2</sub>/TiO<sub>2</sub> hybrids in photo-oxidation of phenol, *Chem. Eng. J.* 138 (2008) 55–62.
- [40] Q. Xiang, J. Yu, M. Jaroniec, Synergetic effect of MoS<sub>2</sub> and graphene as cocatalysts for enhanced photocatalytic H<sub>2</sub> production activity of TiO<sub>2</sub> nanoparticles, *J. Am. Chem. Soc.* 134 (2012) 6575–6578.
- [41] H.-W. Shim, D.K. Lee, I.-S. Cho, K.S. Hong, D.-W. Kim, Facile hydrothermal synthesis of porous TiO<sub>2</sub> nanowire electrodes with high-rate capability for Li ion batteries, *Nanotechnology* 21 (2010) 255706.
- [42] Z. Yin, Z. Zeng, J. Liu, Q. He, P. Chen, H. Zhang, Memory devices using a mixture of MoS<sub>2</sub> and graphene oxide as the active layer, *Small* 9 (2013) 727–731.
- [43] K.C.J. Lee, Y.-H. Chen, H.-Y. Lin, C.-C. Cheng, P.-Y. Chen, T.-Y. Wu, M.-H. Shih, K.-H. Wei, L.-J. Li, C.-W. Chang, Plasmonic gold nanorods coverage influence on enhancement of the photoluminescence of two-dimensional MoS<sub>2</sub> monolayer, *Sci. Rep.* 5 (2015) 16374.
- [44] B. Santara, P.K. Giri, K. Imakita, M. Fujii, Evidence of oxygen vacancy induced room temperature ferromagnetism in solvothermally synthesized undoped TiO<sub>2</sub> nanoribbons, *Nanoscale* 5 (2013) 5476.
- [45] W. Ho, J.C. Yu, J. Lin, J. Yu, P. Li, Preparation and photocatalytic behavior of MoS<sub>2</sub> and WS<sub>2</sub> nanocluster sensitized TiO<sub>2</sub>, *Langmuir* 20 (2004) 5865–5869.
- [46] X. Wang, J. Ding, S. Yao, X. Wu, Q. Feng, Z. Wang, B. Geng, High supercapacitor and adsorption behaviors of flower-like MoS<sub>2</sub> nanostructures, *J. Mater. Chem. A* 2 (2014) 15958–15963.
- [47] K.K. Paul, P.K. Giri, Plasmonic metal and semiconductor nanoparticle decorated TiO<sub>2</sub>-based photocatalysts for solar light driven photocatalysis, Reference Module in Chemistry, Molecular Sciences and Chemical Engineering, Elsevier, 2017.
- [48] D. Hou, W. Zhou, X. Liu, K. Zhou, J. Xie, G. Li, S. Chen, Pt nanoparticles/MoS<sub>2</sub> nanosheets/carbon fibers as efficient catalyst for the hydrogen evolution reaction, *Electrochim. Acta* 166 (2015) 26–31.
- [49] Y. Li, H. Wang, L. Xie, Y. Liang, G. Hong, H. Dai, MoS<sub>2</sub> nanoparticles grown on graphene: an advanced catalyst for the hydrogen evolution reaction, *J. Am. Chem. Soc.* 133 (2011) 7296–7299.
- [50] S. Pal, K.K. Tadi, P.M. Sudeep, S. Radhakrishnan, T.N. Narayanan, Temperature assisted shear exfoliation of layered crystals for the large-scale synthesis of catalytically active luminescent quantum dots, *Mater. Chem. Front.* 1 (2017) 319–325.
- [51] S. Pal, M. Sahoo, V.T. Veettil, K.K. Tadi, A. Ghosh, P. Satyam, R.K. Biroju, P.M. Ajayan, S.K. Nayak, T.N. Narayanan, Covalently connected carbon nanotubes as electrocatalysts for hydrogen evolution reaction through band engineering, *ACS Catalysis* 7 (2017) 2676–2684.
- [52] R.K. Biroju, D. Das, R. Sharma, S. Pal, L.P.L. Mawlong, K. Bhorkar, P.K. Giri, A.K. Singh, T.N. Narayanan, Hydrogen evolution reaction activity of graphene–MoS<sub>2</sub> van der Waals heterostructures, *ACS Energy Lett.* 2 (2017) 1355–1361.
- [53] B. Ma, P.-Y. Guan, Q.-Y. Li, M. Zhang, S.-Q. Zang, MOF-derived flower-like MoS<sub>2</sub>@TiO<sub>2</sub> nanohybrids with enhanced activity for hydrogen evolution, *ACS Appl. Mater. Interfaces* 8 (2016) 26794–26800.
- [54] L. Liao, J. Zhu, X. Bian, L. Zhu, M.D. Scanlon, H.H. Girault, B. Liu, MoS<sub>2</sub> formed on mesoporous graphene as a highly active catalyst for hydrogen evolution, *Adv. Funct. Mater.* 23 (2013) 5326–5333.
- [55] K.B. Ravi, P. Shubhadeep, S. Rahul, P.K. Giri, N.N. Tharangattu, Stacking sequence dependent photo-electrocatalytic performance of CVD grown MoS<sub>2</sub> /graphene van der Waals solids, *Nanotechnology* 28 (2017) 085101.
- [56] S. Xiaolin, C. Guifeng, G. Lixiu, Z. Hui, T. Junguang, Interfacial engineering of MoS<sub>2</sub> /TiO<sub>2</sub> hybrids for enhanced electrocatalytic hydrogen evolution reaction, *Appl. Phys. Express* 9 (2016) 095801.